IOP Publishing | International Atomic Energy Agency Nuclear Fusion

Nucl. Fusion **57** (2017) 116026 (9pp) https://doi.org/10.1088/1741-4326/aa7cab

Enhanced reproducibility of L-mode plasma discharges via physics-model-based *q*-profile feedback control in DIII-D

E. Schuster[1], W.P. Wehner[1], J.E. Barton[1], M.D. Boyer[1], T.C. Luce[2], J.R. Ferron[2], C.T. Holcomb[2], M.L. Walker[2], D.A. Humphreys[2], W.M. Solomon[2], B.G. Penaflor[2] and R.D. Johnson[2]

[1] Lehigh University, Bethlehem, PA 18015-3085, United States of America
[2] General Atomics, San Diego, CA 92186-5608, United States of America

E-mail: schuster@lehigh.edu

Received 5 January 2017, revised 14 June 2017
Accepted for publication 30 June 2017
Published 9 August 2017

Abstract

Recent experiments on DIII-D demonstrate the potential of physics-model-based q-profile control to improve reproducibility of plasma discharges. A combined feedforward + feedback control scheme is employed to optimize the current ramp-up phase by consistently achieving target q profiles (Target 1: $q_{\min} = 1.3, q_{95} = 4.4$; Target 2: $q_{\min} = 1.65, q_{95} = 5.0$; Target 3: $q_{\min} = 2.1, q_{95} = 6.2$) at prescribed times during the plasma formation phase (Target 1: $t = 1.5$ s; Target 2: $t = 1.3$ s; Target 3: $t = 1.0$ s). At the core of the control scheme is a nonlinear, first-principles-driven, physics-based, control-oriented model of the plasma dynamics valid for low confinement (L-mode) scenarios. To prevent undesired L-H transitions, a constraint on the maximum allowable total auxiliary power is imposed in addition to the maximum powers for the individual heating and current-drive sources. Experimental results are presented to demonstrate the effectiveness of the combined feedforward + feedback control scheme to consistently achieve the desired target profiles at the predefined times. These results also show how the addition of feedback control significantly improves upon the feedforward-only control solution by reducing the matching error and also how the feedback controller is able to reduce the matching error as the constraint on the maximum allowable total auxiliary power is relaxed while keeping the plasma in L-mode.

Keywords: plasma control, current profile control, model-based optimization, enhanced discharge reproducibility

(Some figures may appear in colour only in the online journal)

1. Introduction

Reliable reproduction of plasma conditions is critical to conduct meaningful experiments in present devices. This is particularly important for high-$q_{\min}$ steady-state scenarios, which are very sensitive to early changes in the q profile. The potential of model-based q-profile control, particularly during the early ramp-up phase, to improve reproducibility of plasma discharges has been recently demonstrated in experiments on DIII-D. In the absence of feedback control, variability in wall conditions and plasma impurities, as well as drifts due to external plasma disturbances, can limit the reproducibility of discharges attained with simple pre-programmed scenario trajectories. A combined feedforward + feedback control scheme [1] has been employed to optimize the current ramp-up phase by consistently achieving target q profiles at prescribed times in L-mode discharges. The scheme incorporates the physics of the to-be-controlled system by embedding a control-oriented plasma-response model in the control design. Experiments show that feedback control significantly improves upon the feedforward-only control solution by reducing the matching error between actual and target profiles.

A nonlinear, physics-based, control-oriented model of the plasma dynamics enables the design of effective current-profile control algorithms. Work towards control-oriented modeling for current-profile control design started almost a decade ago with the pioneering work in [2] and [3]. The physics information contained in the nonlinear model is embedded into the feedforward and feedback components of the control scheme through advanced model-based control design techniques. Firstly, a nonlinear, constrained optimization algorithm is developed to design feedforward actuator trajectories with the goal of numerically complementing the traditional trial-and-error experimental effort of advanced scenario planning. The idea of combining predictive simulation with optimization techniques for model-based scenario planning was originally proposed in [4–7] by employing different approaches such as extremum seeking, iterative learning control, minimal surface theory and sequential quadratic programming. The goal of the optimization algorithm is to design actuator trajectories that steer the plasma to the target q profile at a predefined time subject to the plasma dynamics and plasma state and actuator constraints, such as the minimum q value and the maximum available auxiliary heating and current-drive (H&CD) power. Secondly, integrated feedback control algorithms are designed to keep the q-profile evolution on track by countering the effects of external plasma disturbances and unmodeled dynamics, thereby adding robustness to the control scheme. Optimal [8], robust [9, 10] and backstepping [11] controllers have been employed in this work to achieve this goal. The H&CD system and the total plasma current are the actuators utilized by the feedback controllers to control the plasma dynamics. To ensure the discharge remains in L-mode, maximum allowable auxiliary power constraints are imposed on both the feedforward and the feedback controllers.

This paper is organized as follows. In section 2, a first-principles-driven (FPD) model of the plasma current profile dynamics is developed. The modeling process starts by considering the well known one-dimensional poloidal magnetic flux diffusion equation, which describes the resistive diffusion of the poloidal magnetic flux in the tokamak in response to the electric field due to induction, the noninductive current driven by the auxiliary H&CD system, and the neoclassical bootstrap effect. This first-principles model is subsequently converted into a form suitable for control design by developing control-oriented versions of physics-based models of the electron density, the electron temperature, the plasma resistivity, and the noninductively driven currents (auxiliary and bootstrap) in response to the control actuators. In section 3, the developed FPD model is embedded into a numerical optimization algorithm to design actuator trajectories that steer the plasma state to achieve a desired q profile at a given time. The optimized trajectories are subsequently tested experimentally in DIII-D. In section 4, feedback control of the q profile is added to the feedforward control solution by following an FPD model-based control design approach based on different techniques. The ability of the overall feedforward + feedback q profile controller to achieve a desired q profile at a predefined time is assessed in DIII-D L-mode experiments. Finally, conclusions are discussed in section 5.

2. Model-based control architecture

The used *model-based* control architecture is a *feedforward + feedback* scheme where the feedforward commands are computed off-line and the feedback commands are computed on-line taking into account *auxiliary-power constraints* to keep the plasma in L-mode.

2.1. Control-oriented plasma response model

At the core of the developed control algorithms is a nonlinear, physics-based, control-oriented model that captures the response of the plasma (q-profile) to the control actuators (total plasma current (I_p), line average electron density ($\bar{n}_e$), auxiliary electron cyclotron (EC) power (P_ec), and auxiliary neutral beam injection (NBI) power (P_nbi)). The DIII-D auxiliary H&CD actuators considered in this work are 6 gyrotrons, which are grouped together to form 1 effective EC source for control, 6 individual co-current NBI sources [30L/R,150L/R,330L/R], and 2 individual counter-current NBI sources [210L/R], where L and R denote left and right lines, respectively. The 150L/R NBI lines are utilized as off-axis H&CD sources, while the 30L/R, 210L/R and 330L/R NBI lines are utilized as on-axis H&CD sources. The evolution of the poloidal magnetic flux profile, which is closely related to the q-profile, is given by the magnetic diffusion equation [12]

$$\frac{\partial\psi}{\partial t} = \frac{\eta}{\mu_0\rho_b^2\hat{F}^2}\frac{1}{\hat{\rho}}\frac{\partial}{\partial\hat{\rho}}\left(\hat{\rho}\hat{F}\hat{G}\hat{H}\frac{\partial\psi}{\partial\hat{\rho}}\right) + R_0\hat{H}\eta\frac{\langle\bar{j}_\mathrm{ni}\cdot\bar{B}\rangle}{B_{\phi,0}}, \tag{1}$$

with boundary conditions

$$\left.\frac{\partial\psi}{\partial\hat{\rho}}\right|_{\hat{\rho}=0} = 0 \qquad \left.\frac{\partial\psi}{\partial\hat{\rho}}\right|_{\hat{\rho}=1} = -\frac{\mu_0}{2\pi}\frac{R_0}{\hat{G}\big|_{\hat{\rho}=1}\hat{H}\big|_{\hat{\rho}=1}}I_\mathrm{p}(t). \tag{2}$$

The poloidal stream function ψ is closely related to the poloidal magnetic flux Ψ ($\Psi = 2\pi\psi$), t is the time, η is the plasma resistivity, μ_0 is the vacuum magnetic permeability, $\langle\bar{j}_\mathrm{ni}\cdot\bar{B}\rangle/B_{\phi,0}$ is any source of noninductive current density, and I_p is the total plasma current. The spatial coordinate $\hat{\rho} = \rho/\rho_b$ (normalized effective minor radius) indexes the plasma magnetic flux surfaces, where ρ is the effective minor radius of a magnetic flux surface, i.e. $\Phi(\rho) = \pi B_{\phi,0}\rho^2$, Φ is the toroidal magnetic flux, $B_{\phi,0}$ is the vacuum toroidal magnetic field at the geometric major radius R_0 of the tokamak, and ρ_b is the effective minor radius of the last closed magnetic flux surface. The spatial profiles $\hat{F}$, $\hat{G}$ and $\hat{H}$ are geometric factors pertaining to the magnetic configuration of a particular plasma equilibrium (see [13] for instance), and are defined as,

$$\hat{F}(\hat{\rho}) = \frac{R_0B_{\phi,0}}{RB_\phi}, \quad \hat{G}(\hat{\rho}) = \left\langle\frac{R_0^2}{R^2}|\nabla\rho|^2\right\rangle, \quad \hat{H}(\hat{\rho}) = \frac{\hat{F}}{\langle R_0^2/R^2\rangle}, \tag{3}$$

where R denotes the radial spatial coordinate in the poloidal plane of the tokamak, B_ϕ is the toroidal magnetic field, and $\langle\cdot\rangle$ denotes the flux-surface average operation $\frac{\partial}{\partial V}\int_V(\cdot)\mathrm{d}V$ where V is the volume enclosed by a magnetic flux surface.

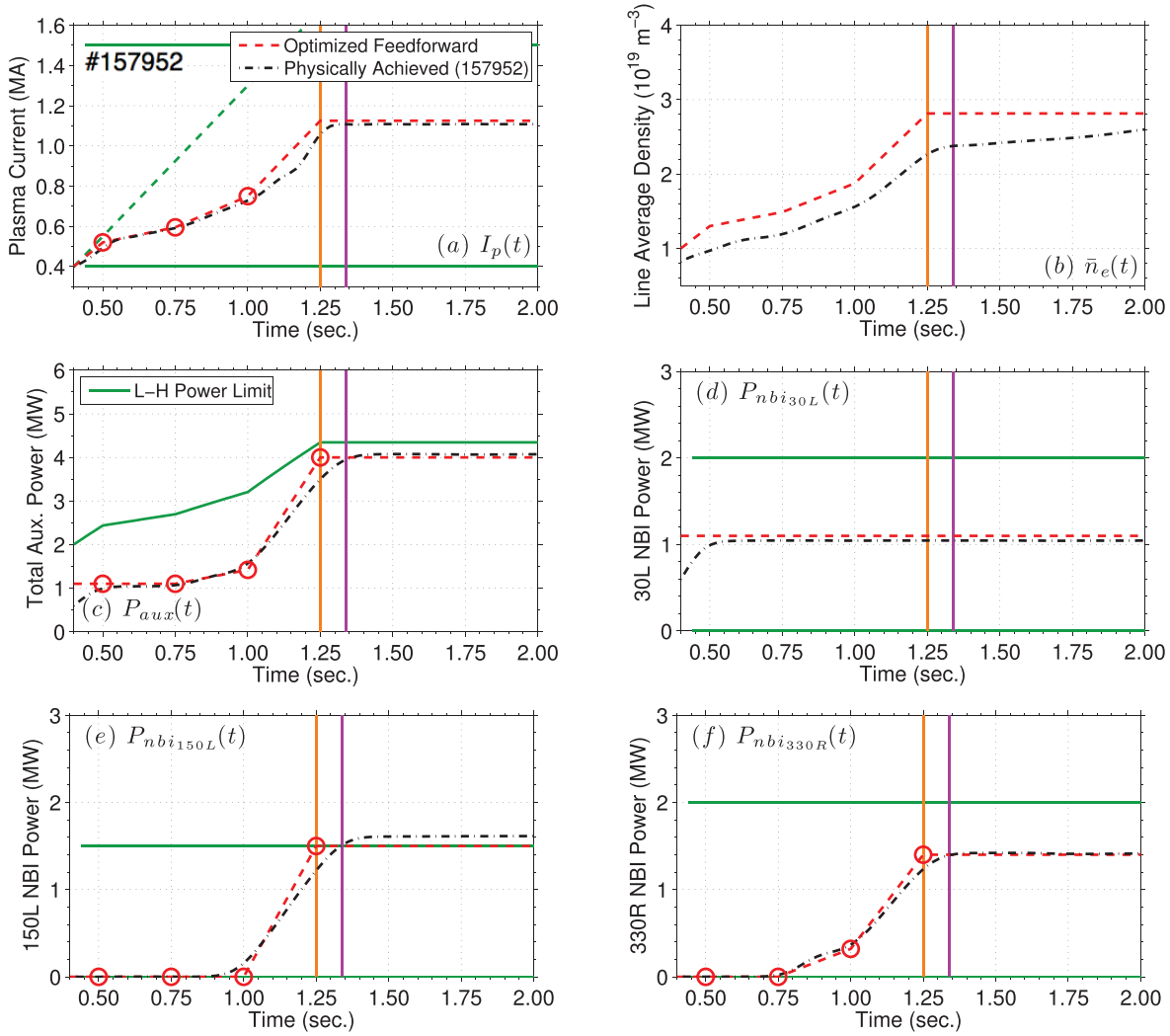

Figure 1. Optimized feedforward actuator trajectories for (*a*) I_p; (*b*) $\bar{n}_e$; (*c*) P_{aux}; (*d*) P_{NBI}^{30L}; (*e*) P_{NBI}^{150L}; (*d*) P_{NBI}^{330R}. Optimized actuator parameters (red circled), optimized actuator trajectories (red dashed), physically achieved actuator trajectories (black dashed), actuator saturation values (green solid), actuator rate limits (green dashed), simulation best target matching time (orange), and experimental best target matching time (purple).

A first-principles-driven (FPD) control-oriented model of the evolution of the poloidal flux profile, and hence the safety-factor profile

$$q(\hat{\rho},t) = -\frac{\mathrm{d}\Phi}{\mathrm{d}\Psi} = -\frac{\mathrm{d}\Phi}{2\pi \mathrm{d}\psi} = -\frac{B_{\phi,0}\rho_b^2\hat{\rho}}{\partial\psi/\partial\hat{\rho}}, \tag{4}$$

is developed by combining (1) with physics-based models of the electron density, the electron temperature, the plasma resistivity, and the noninductive current sources [2, 14].

2.1.1. Electron density modeling. In the formulation of the electron density model, it is assumed that the control action employed to regulate the electron density only weakly affects the radial distribution of the electrons. Therefore, the electron density evolution $n_e(\hat{\rho},t)$ is modeled as

$$n_e(\hat{\rho},t) = n_e^{\mathrm{prof}}(\hat{\rho})\bar{n}_e(t), \tag{5}$$

where $n_e^{\mathrm{prof}}(\hat{\rho})$ is a reference electron density profile and $\bar{n}_e(t)$ is the line average electron density, which is typically utilized to specify the electron density in present tokamak operation.

2.1.2. Electron temperature modeling. To model the electron temperature profile evolution, an approximate singular perturbation approach is employed by exploiting the fact that the characteristic thermal diffusion time in the plasma is much faster than the characteristic resistive diffusion time. Therefore the temperature is always in quasi-equilibrium on the time-scale of the current evolution, and we neglect the temporal dynamics of the electron temperature in the development of the electron temperature evolution model as we are mainly concerned with capturing the dominant physical effects that the electron temperature has on the plasma magnetic profile evolution. Therefore, the fast evolving (on the resistive current diffusion time scale) electron temperature profile evolution $T_e(\hat{\rho},t)$ is modeled as

$$T_e(\hat{\rho},t) = T_e^{\mathrm{prof}}(\hat{\rho})I_{\mathrm{p}}(t)^{\gamma}P_{\mathrm{tot}}(t)^{\varepsilon}\bar{n}_e^{\zeta}, \tag{6}$$

where $T_e^{\mathrm{prof}}(\hat{\rho})$ is a reference electron temperature profile and γ, ε, ζ are scaling constants. To arrive at the scaling shown in (6), first a steady-state, zero-dimensional plasma energy balance is considered, i.e. $W/\tau_W = P_{\mathrm{tot}}$, where $W \propto \langle n_e\rangle\langle T_e\rangle$ is the total

plasma stored energy (assuming $T_i \propto T_e$ and $n_i \propto n_e$), τ_W is the energy confinement time, $P_{\rm tot} = P_{\rm ohm} + P_{\rm aux} - P_{\rm rad}$ is the total power density, $P_{\rm ohm}$ is the ohmic power density, $P_{\rm aux}$ is the total auxiliary H&CD power density, and $P_{\rm rad}$ is the radiated power density. Many energy confinement scaling laws have been developed over the years, and typically these scaling laws are functions of the actuators used for plasma control, i.e. $\tau_W \propto I_{\rm p}^{\gamma_s} P_{\rm tot}^{\varepsilon_s} \langle n_e \rangle^{\zeta_s}$, where γ_s, ε_s and ζ_s depend on the particular scaling law used. The scaling in the electron temperature model shown in (6) is inspired by the form of T_e when the steady-state zero-dimensional energy balance equation is solved assuming the above scaling law, i.e. $\langle T_e \rangle \propto \langle n_e \rangle^{-1} \tau_W P_{\rm tot} \propto I_{\rm p}^{\gamma} P_{\rm tot}^{\varepsilon} \langle n_e \rangle^{\zeta}$ with $\gamma = \gamma_s$, $\varepsilon = 1 + \varepsilon_s$ and $\zeta = \zeta_s - 1$. Values of $\gamma = 1$, $\varepsilon = 0.5$, and $\zeta = -1$ have been adopted in this work.

2.1.3. Plasma resistivity modeling. Following a simplified Spitzer resistivity model, the plasma resistivity $\eta(T_e)$ scales with the electron temperature as

$$\eta(\hat{\rho}, t) = \frac{k_{\rm sp}(\hat{\rho}) Z_{\rm eff}}{T_e(\hat{\rho}, t)^{3/2}}, \tag{7}$$

where $k_{\rm sp}(\hat{\rho})$ is a scaling profile. We neglect neoclassical corrections to this formula, which can nonetheless be significant, to retain the main dependence.

2.1.4. Noninductive current-drive modeling. The total noninductive current-drive is expressed as

$$\frac{\langle \bar{j}_{\rm ni} \cdot \bar{B} \rangle}{B_{\phi,0}} = \sum_{i=1}^{n_{\rm ec}} \frac{\langle \bar{j}_{ec_i} \cdot \bar{B} \rangle}{B_{\phi,0}} + \sum_{i=1}^{n_{\rm nbi}} \frac{\langle \bar{j}_{{\rm nbi}_i} \cdot \bar{B} \rangle}{B_{\phi,0}} + \frac{\langle \bar{j}_{\rm bs} \cdot \bar{B} \rangle}{B_{\phi,0}}, \tag{8}$$

where $\bar{j}_{ec_i}$ is the noninductive current generated by the individual gyrotron launchers, $\bar{j}_{{\rm nbi}_i}$ is the noninductive current generated by the individual neutral beam injectors, and $\bar{j}_{\rm bs}$ is the noninductive current generated by the bootstrap effect.

Each auxiliary noninductive current source is modeled as a fixed deposition profile multiplied both by an efficiency term, which is function of the ratio between a power of $T_e(\hat{\rho}, t)$ and $n_e(\hat{\rho}, t)$, and by the time varying power associated to the current source, i.e.

$$\frac{\langle \bar{j}_i \cdot \bar{B} \rangle}{B_{\phi,0}}(\hat{\rho}, t) = j_i^{\rm ref}(\hat{\rho}) \frac{T_e(\hat{\rho}, t)^{\delta}}{n_e(\hat{\rho}, t)} P_i(t), \tag{9}$$

where $i \in [ec_1, \ldots, ec_{n_{ec}}, nbi_1, \ldots, nbi_{n_{nbi}}]$ and $j_i^{\rm ref}(\hat{\rho})$ is a reference deposition profile for each current-drive source. For electron cyclotron current-drive, $\delta = 1$ [15] and for neutral beam current-drive, δ is dependent on the energy of the injected particles [16]. Injected particles in DIII-D have an energy of 80 keV in this work, which leads to $\delta = 1/2$.

The bootstrap current [17] is associated with trapped particles and arises from the inhomogeneity of the magnetic field strength produced by the external coils in the tokamak, which falls off like $1/R$. From [18, 19], the bootstrap current is written as

$$\frac{\langle \bar{j}_{\rm bs} \cdot \bar{B} \rangle}{B_{\phi,0}} = \frac{R B_{\phi}(\psi)}{B_{\phi,0}} p_e \left[\mathscr{L}_{31} \left\{ \frac{1}{p_e} \frac{\partial p_e}{\partial \psi} + \frac{1}{p_e} \frac{\partial p_i}{\partial \psi} \right\} + \mathscr{L}_{32} \frac{1}{T_e} \frac{\partial T_e}{\partial \psi} + \mathscr{L}_{34} \alpha \frac{1 - R_{\rm pe}}{R_{\rm pe}} \frac{1}{T_i} \frac{\partial T_i}{\partial \psi} \right], \tag{10}$$

where p_e denotes the electron pressure, p_i denotes the ion pressure, and $R_{\rm pe} = p_e/p$ where p is the total plasma pressure (note the opposite sign of (10) due to the different definition of ψ). Under working assumptions of a tight coupling between the electron and ion species in the plasma, i.e. $T_e \approx T_i$ and $n_e \approx n_i$, it is possible to write $p_e = n_e T_e = n_i T_i = p_i$ and $R_{\rm pe} = (n_e T_e)/(n_e T_e + n_i T_i) = 1/2$. Substituting these relationships into (10) we obtain

$$\frac{\langle \bar{j}_{\rm bs} \cdot \bar{B} \rangle}{B_{\phi,0}}(\hat{\rho}, t) = \frac{R_0}{\hat{F}(\hat{\rho})} \left(\frac{\partial \psi}{\partial \hat{\rho}} \right)^{-1} \left[2\mathscr{L}_{31}(\hat{\rho}) T_e(\hat{\rho}, t) \frac{\partial n_e}{\partial \hat{\rho}} + \{ 2\mathscr{L}_{31}(\hat{\rho}) + \mathscr{L}_{32}(\hat{\rho}) + \alpha(\hat{\rho}) \mathscr{L}_{34}(\hat{\rho}) \} n_e(\hat{\rho}, t) \frac{\partial T_e}{\partial \hat{\rho}} \right], \tag{11}$$

where the coefficients $\mathscr{L}_{31}(\hat{\rho})$, $\mathscr{L}_{32}(\hat{\rho})$, $\mathscr{L}_{34}(\hat{\rho})$ and $\alpha(\hat{\rho})$ depend on the magnetic configuration of a particular plasma equilibrium and on particle collisionality in the plasma.

2.2. Power limit to prevent L-H transitions

To avoid L-H transitions, a total auxiliary power limit was imposed during the experiments. In early discharges, a fixed power limit failed to prevent transitions to H-mode. The transition power was observed in these experiments to approximately scale with the electron density as

$$P_{\rm LH} = 2\bar{n}_e^{3/4}. \tag{12}$$

Therefore, the total injected power in later discharges was constrained by this limit.

3. Feedforward control via nonlinear programming

Model-based feedforward-only control, as that arising from typical scenario planning work, is able to drive the q profile close to the target in the outer region ($\hat{\rho} > 0.3$) during the experiments. The design of the feedforward control law $u_{\rm FF}$ can be formulated as a nonlinear optimization problem [20], i.e.

$$\begin{aligned} \underset{u_{\rm FF}}{\text{minimize}} \quad & J(\psi(t_{\rm targ}), \psi_{\rm targ}) \\ \text{subject to} \quad & \psi\text{−dynamics governed by (1) and (2)}, \\ & \psi(t_0) \text{ (initial condition)}, \\ & g_0(u_{\rm FF}) \leqslant 0, \;\; g_i(u_{\rm FF}) \leqslant 0 \quad (i = 1, 2, \ldots), \end{aligned} \tag{13}$$

where $\psi_{\rm targ}$ represents the target profile, $t_{\rm targ}$ is the desired time for reaching the target profile, $J(\psi(t_{\rm targ}), \psi_{\rm targ})$ is a quadratic cost function which penalizes deviations from the desired target profile, $g_0(u_{\rm FF})$ is a nonlinear constraint which prevents L-H transition, and $g_i(u_{\rm FF})$ is a set of linear constraints that account for the actuator limits (subindex i denotes different actuators). The solution of the optimization problem (13) is a feedforward control policy given by $u_{\rm FF}$ and a corresponding state reference trajectory predicted by (1) that serves as a path from the initial profile to the target profile.

In this experiment, three target q profiles (Target 1: $q_{\rm min} = 1.3, q_{95} = 4.4$;Target2:$q_{\rm min} = 1.65, q_{95} = 5.0$;Target3: $q_{\rm min} = 2.1, q_{95} = 6.2$) have been prescribed at different times

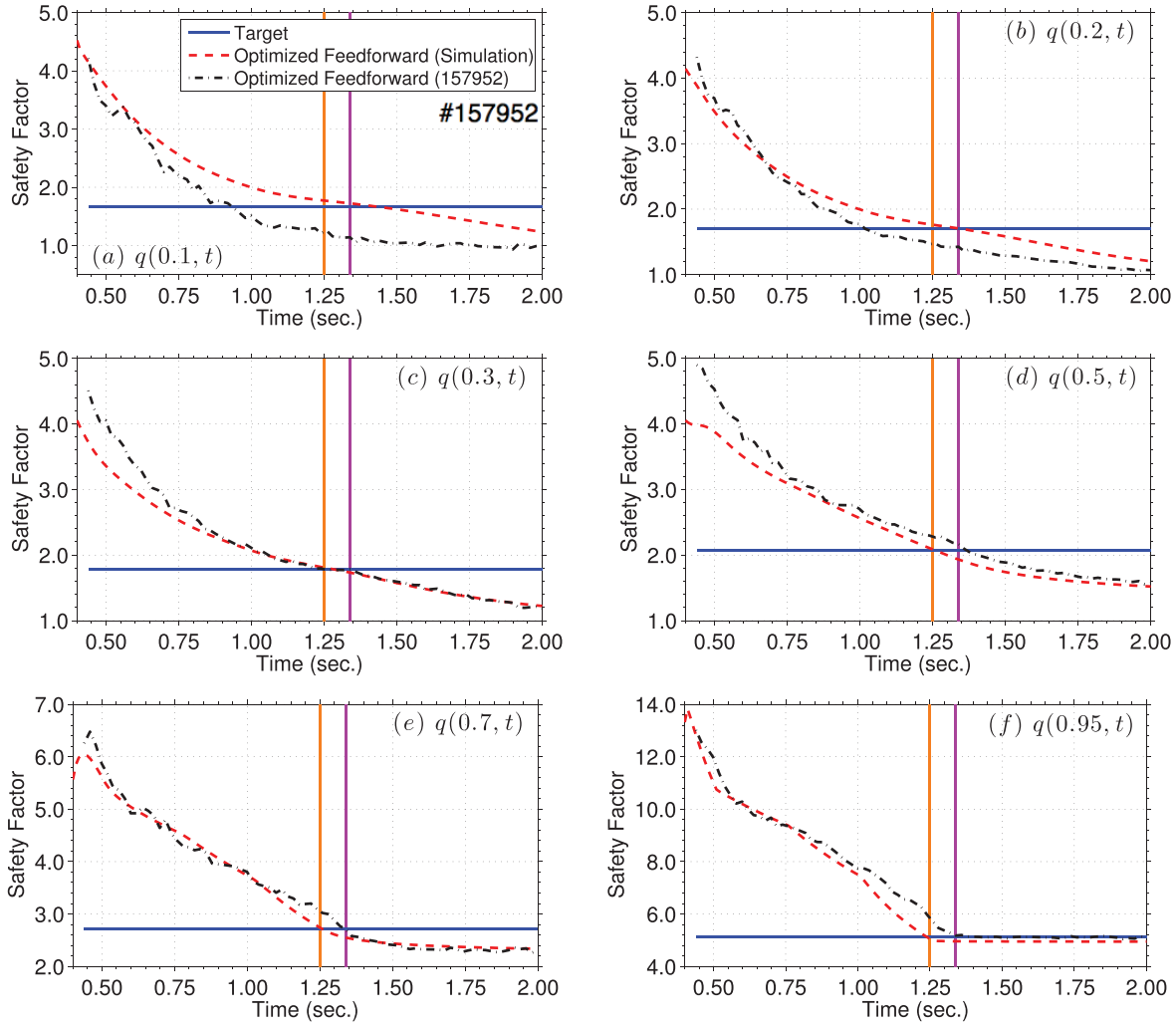

Figure 2. Time traces of q at $\hat{\rho} = 0.1, 0.2, 0.3, 0.5, 0.7, 0.95$. Target (blue solid), simulation (red dashed), experiment (black dashed-dotted), simulation best target matching time (orange), and experimental best target matching time (purple).

during the plasma formation phase (Target 1: $t = 1.5$ s; Target 2: $t = 1.3$ s; Target 3: $t = 1.0$ s). The optimized feedforward actuator trajectories u_{FF} obtained as the solution of problem (13) were tested experimentally in DIII-D. Figure 1 shows these trajectories (red dashed lines) for shot #157952, which are characterized by a variable plasma current ramp-up rate and a late application of auxiliary NBI power up to the maximum value. The flattop plasma current is constrained to a fixed value. The line average density is fixed and proportional to the plasma current, i.e. $\bar{n}_e(t)[10^{19}\ \mathrm{m}^{-3}] = 2.5 I_{\mathrm{p}}(t)$ [MA]. The 30 L NBI power is fixed at 1.1 MW (necessary for diagnostics). The physically achieved actuator trajectories (black dashed-dotted lines) show some time delay with respect to the optimized feedforward trajectories[3], which results in a best-matching time (1.339 s) slightly larger than the target time (1.25 s) for Target 2 as shown in figure 2. Comparison of experimental (black dashed-dotted lines) and simulated (red dashed lines) q-profile evolutions in figure 2 indicates that the current density diffuses towards the plasma core faster than predicted by the FPD control-oriented model. This can also be appreciated in figure 3, where the experimentally achieved q profile (black dashed-dotted line) is compared with its target (green circled lines) for different discharges (Target 1 in shot #157947, Target 2 in shots #157948 and #157952, and Target 3 in shot #157949). Reduction of the mismatch, particularly in the inner region, demands on-line feedback control.

4. Feedback controller for robust target q-profile matching

The addition of a feedback control component adds robustness to the overall control scheme and proves itself capable of consistently driving the q profile to its target in these experiments. The feedforward control law needs to be complemented by a feedback control law in order to mitigate deviations from

[3] The optimized feedforward actuator trajectories u_{FF} are indeed references passed to the dedicated controllers for the plasma current, plasma density and H&CD source powers. Therefore, there is no guarantee that the optimized feedforward actuator trajectories can actually be replicated in experiments, which makes offsets and delays possible as observed in these experiments.

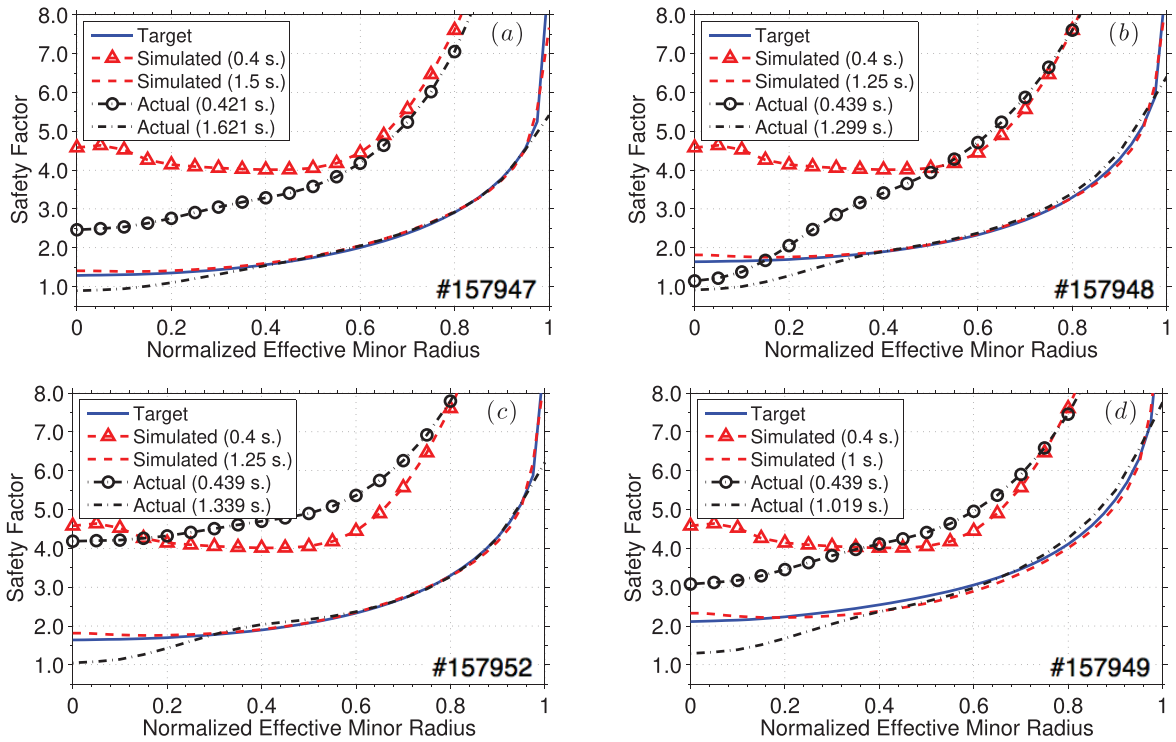

Figure 3. Best q profile target matching for optimized feedforward experiments; target (blue solid), simulated best match (red dashed), and experimental best match (black dashed-dotted): (a) Target 1, (b) and (c) Target 2, (d) Target 3. Simulation and experimental initial profiles are represented by red dashed-triangled and black dashed-circled lines, respectively.

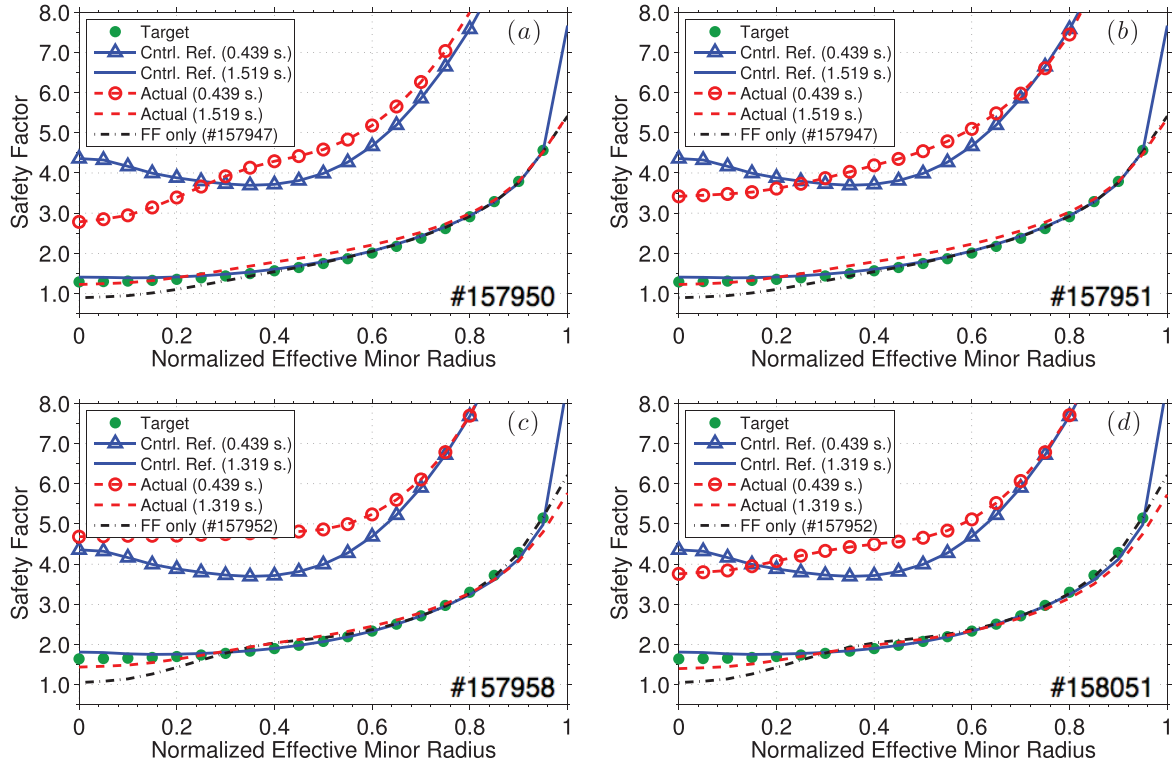

Figure 4. Experimental testing of feedforward + feedback q-profile control scheme for Target 1 and Target 2: ((a) and (b)) Initial ($t = 439$ ms, red dashed-circled line) and final ($t = 1519$ ms, red dashed line) q-profiles for Target 1 shots #157950 and #157951; ((c) and (d)) Initial ($t = 439$ ms, red dashed-circled line) and final ($t = 1319$ ms, red dashed line) q-profiles for Target 2 shots #157958 and #158051.

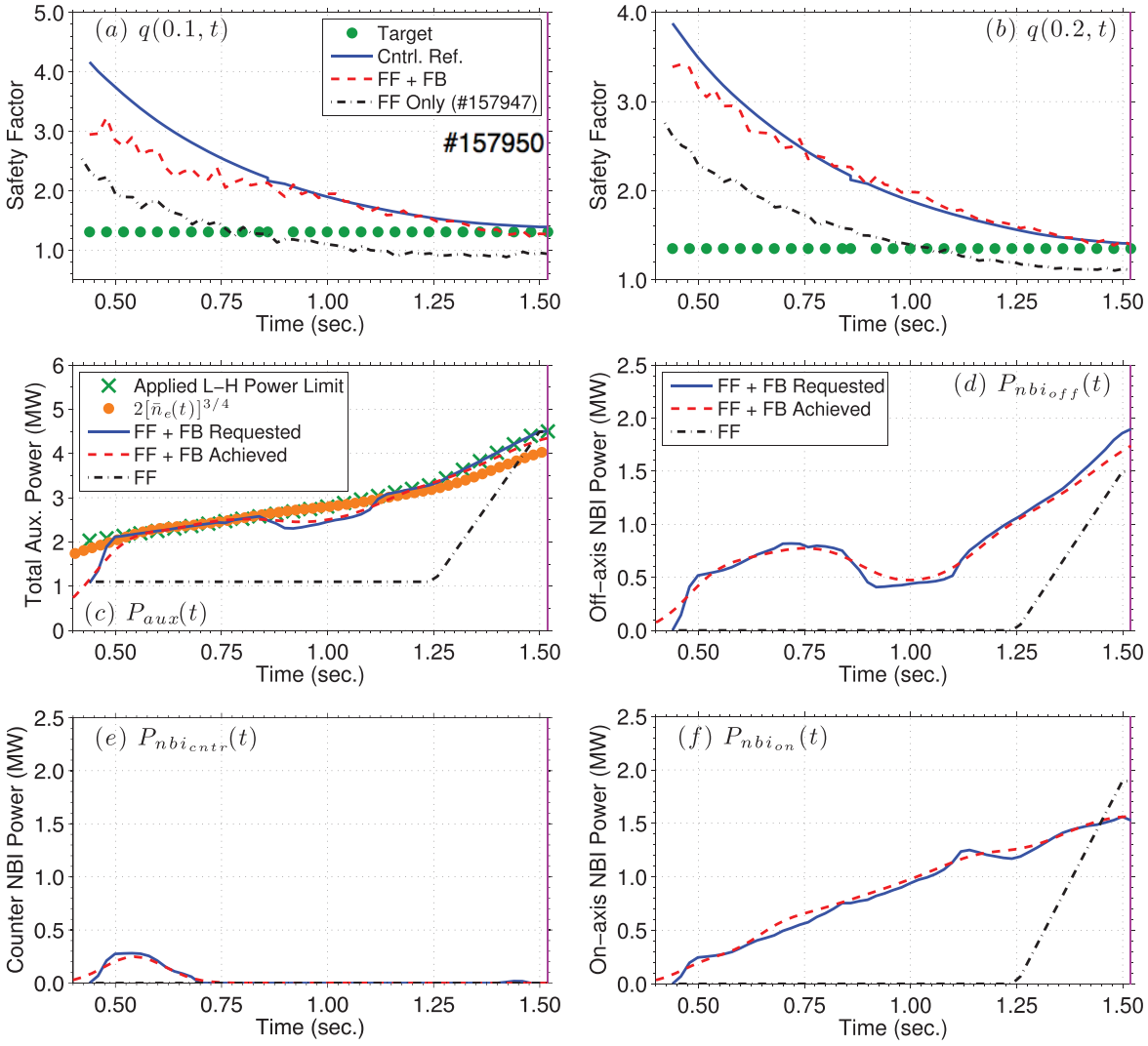

Figure 5. ((*a*) and (*b*)) Time traces of q at $\hat{\rho} = 0.1$ and $\hat{\rho} = 0.2$: target (green circled), control reference (blue solid), FF + FB (red dashed), FF (black dashed-dotted); ((*c*)–(*f*)) Comparison of actuator trajectories: applied total auxiliary power limit (green crossed), $P_{\rm LH}$ scaling (orange circled), FF + FB requested power (blue solid), FF + FB achieved power (red dashed), FF achieved power (black dashed-dotted).

the desired state reference trajectory due to perturbations in the initial condition, external disturbances, and unmodeled dynamics. Three feedback control algorithms were employed in these experiments, which were designed based on optimal control [8, 21], robust control [1, 9, 10], and backstepping control [11] design techniques. The feedback portion of the controller was interfaced with the real-time EFIT (rtEFIT) equilibrium reconstruction code [22]. The q profile is computed by rtEFIT based on motional Stark effect (MSE) diagnostic measurements. The plasma variables provided to the plasma control system (PCS) by rtEFIT are the plasma current $I_{\rm p}$, the poloidal stream function at the magnetic axis ψ_{axis} and at the plasma boundary $\psi_{\rm bdry}$, and the safety factor q at 65 evenly spaced points on the normalized-ψ spatial domain. These measurements are used by the PCS to compute the q profile at 20 evenly spaced points on the normalized-ρ spatial domain. The q profile was computed every 20 ms. This sampling time was set based on the modulation of the MSE (30 L) beam used to obtain q-profile measurements in real-time. In this case the MSE beam was modulated on for 10 ms then off for 10 ms. The achieved feedback-controlled profiles (dashed red lines) are compared with the targets in both figures 4 and 6, showing a significant and consistent matching improvement. To allow for a better comparison, all the shots presented in this section were achieved using the same type of robust-control algorithm [1, 9, 10].

Figures 4(*a*) and (*b*) show how the combined feedforward + feedback controller is capable of repeatedly achieving Target 1 at the predefined time of approximately 1.5 s in shots #157950 and #157951. Repeatability of the plasma discharge is indeed one of the key performance metrics that model-based feedback control has the potential of improving. These figures also illustrate the performance of the feedforward-only controller in shot #157947. The feedback component of the control scheme compensates for the faster-than-model-predicted (used to obtain the feedforward control laws) current density diffusion in the inner region and improves profile matching. Figure 5(*a*) shows in detail how the feedforward + feedback controller drives the actual value of q at $\hat{\rho} = 0.1$ (dashed red line) to its reference (solid

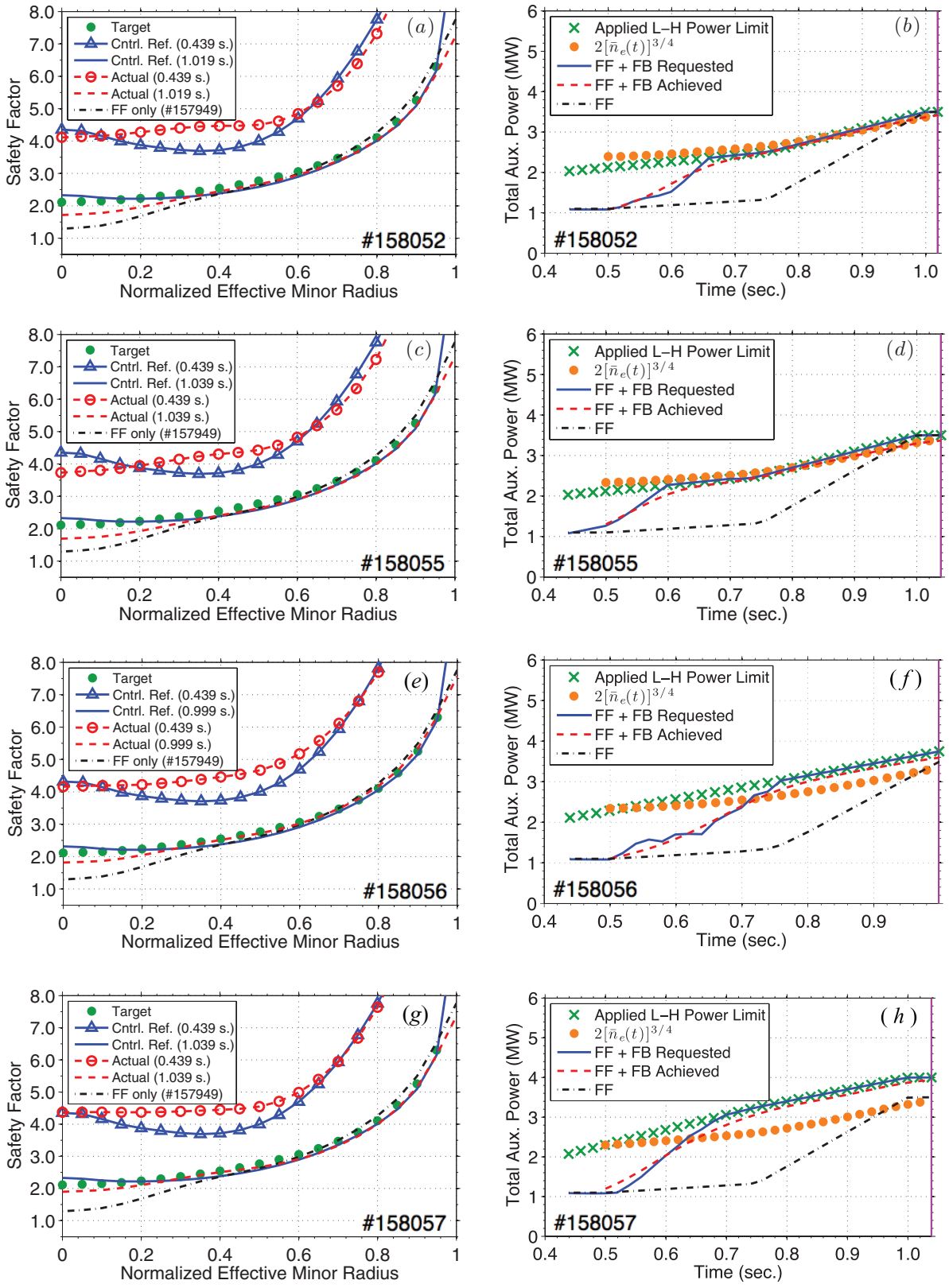

Figure 6. Experimental testing of feedforward + feedback q-profile control for Target 3: ((*a*), (*c*), (*e*) and (*g*)) Initial ($t = 439$ ms, red dashed-circled line) and final ($t \approx 1000$ ms, red dashed line) q-profiles for Target 3 shots #158052, #158055, #158056 and #158057; ((*b*), (*d*), (*e*) and (*h*)) Time evolution of total auxiliary power. The orange circled lines denote the power-limit scaling P_{LH} while the green crossed lines denote the actual applied power limit. Feedforward-only actuator trajectories are shown in black dashed-dotted lines, while both requested and achieved feedforward + feedback actuator trajectories are shown in solid blue and dashed red lines, respectively.

blue line), which in turn converges to its associated target value (circled green line) at the desired target time of 1.5 s, and improves upon the matching obtained by the feedfoward-only q evolution (dashed-dotted black line) extracted from shot #157947, which hits the target much earlier than sought. This is achieved by increasing the total auxiliary power (red dashed line) in comparison with the feedforward-only total auxiliary power (black dashed-dotted line) as shown in figure 5(*b*). Figures 4(*c*) and (*d*) demonstrates how the feedforward + feedback controller can achieve different target profiles at different target times. In this case, Target 2 is achieved in shots #157958 and #158051 at the predefined time of approximately 1.3 s much more precisely than in shot#157952, where feedback actuation was absent.

Figure 6 shows the effectiveness of the combined feedforward + feedback control scheme to achieve Target 3 at approximately 1 s. Figures 6(*a*) and (*c*) shows that the controller achieves almost identical matching performance for shots #158052 and #158055, characterized by slightly different initial profiles at 439 ms (red dashed-circled lines), by actuating the plasma in a slightly different manner as shown in figures 6(*b*) and (*d*). This is a key result of the experiment, where repeatability of the plasma discharge was sought. As can be noted from figures 6(*a*) and (*c*), while the feedfoward + feedback controller improves upon the matching obtained by the feedforward-only controller in the inner region (shot #157949), the achieved matching in these Target 3 shots is not as good as those observed for Target 1 and Target 2 shots in figure 4 (note from figure 4 that matching for Target 2 is already not as good as for Target 1). The explanation for this behavior can be found in figures 6(*b*) and (*d*), where it can be noted that the actuation requested by the controller (solid blue line), as well as the actuation actually achieved by the actuators (dashed red line), are constrained very early in the discharge by the power limit (crossed green line) imposed on the controller in order to prevent undesirable L-H transitions. This power limit follows closely the power scaling (orange circled line) obtained as part of this experiment for L-H transitions, which is given in (12). With the purpose of improving the matching in the inner region, the applied power limit was slowly moved beyond the power scaling P_{LH} in shots #158056 and #158057. As can be appreciated from figures 6(*e*) and (*g*), the matching is consistently improved as the power limit is increased as shown in figures 6 (*f*) and (*h*). The power scaling P_{LH} was proved conservative and profile matching was improved while staying in L mode. However, although at a higher level and at a later time, the controller still reached auxiliary-power saturation in shots #158056 and #158057. This indicates that further matching improvement might be possible by increasing the power limit but at the risk of possibly transitioning to H mode.

5. Conclusions and future work

These experiments demonstrate the capability of model-based profile control to improve scenario robustness, thereby providing significantly improved main operating regimes for steady-state studies in DIII-D. During upcoming DIII-D campaigns, this approach will be extended to H-mode by simultaneously controlling the q-profile and β_N in feedforward + feedback control experiments. One of the goals will be to determine if the same level of startup-phase optimization as that achieved in L-mode (first stage of control development) is indeed attainable with the present actuation capability in lower-resistivity H-mode plasmas.

Acknowledgment

This material is based upon work partly supported by the U.S. Department of Energy, Office of Science, Office of Fusion Energy Sciences, using the DIII-D National Fusion Facility, a DOE Office of Science user facility, under Awards DE-SC0001334, DE-SC0010661, and DE-FC02-04ER54698. DIII-D data shown in this paper can be obtained in digital format by following the links at https://fusion.gat.com/global/D3D_DMP

References

[1] Barton J. *et al* 2015 *Nucl. Fusion* **55** 093005
[2] Ou Y. *et al* 2007 *Fusion Eng. Des.* **82** 1153
[3] Witrant E. *et al* 2007 *Plasma Phys. Control. Fusion* **49** 1075
[4] Ou Y. *et al* 2008 *Plasma Phys. Control. Fusion* **50** 115001
[5] Xu C., Arastoo R. and Schuster E. 2009 On iterative learning control of parabolic distributed parameter systems *Proc. 17th Mediterranean Conf. on Control and Automation (Thessaloniki, Greece, 24–26 June 2009)*
[6] Xu C. and Schuster E. 2009 Control of ramp-up current profile dynamics in tokamak plasmas via the minimal-surface theory *Proc. 48th IEEE Conf. on Decision and Control (Shanghai, China, 16–18 December 2009)*
[7] Xu C. *et al* 2010 *IEEE Trans. Plasma Sci.* **38** 163
[8] Boyer M.D. *et al* 2013 *Plasma Phys. Control. Fusion* **55** 105007
[9] Barton J. *et al* 2012 *Nucl. Fusion* **52** 123018
[10] Barton J., Besseghir K., Lister J. and Schuster E. 2015 *Plasma Phys. Control. Fusion*
[11] Boyer M. *et al* 2014 *IEEE Trans. Control Syst. Technol.* **22** 1725
[12] Hinton F.L. and Hazeltine R.D. 1976 *Rev. Mod. Phys.* **48** 239
[13] St John H. http://fusion.gat.com/THEORY/onetwo/
[14] Barton J.E. *et al* 2013 Physics-based control-oriented modeling of the safety factor profile dynamics in high performance tokamak plasmas *Proc. 52nd IEEE Conf. on Decision and Control (Florence, Italy, 10–13 December 2013)*
[15] Luce T.C. *et al* 1999 *Phys. Rev. Lett.* **83** 4550
[16] Politzer P.A. and Porter G.D. 1990 *Nucl. Fusion* **30** 1605
[17] Peeters A.G. 2000 *Plasma Phys. Control. Fusion* **42** B231
[18] Sauter O. *et al* 1999 *Phys. Plasmas* **6** 2834
[19] Sauter O. *et al* 2002 *Phys. Plasmas* **9** 5140
[20] Barton J. *et al* 2014 Nonlinear physics-model-based actuator trajectory optimization for advanced scenario planning in the DIII-D tokamak *Proc. 19th IFAC World Congress (Cape Town, South Africa, 24–29 August 2014)*
[21] Wehner W. *et al* 2015 Current profile control for the development of consistent discharges in DIII-D *Proc. of the 54th IEEE Conf. on Decision and Control (Osaka, Japan, 15–18 December 2015)*
[22] Ferron J.R. *et al* 1998 *Nucl. Fusion* **38** 1055